Energy Meteorology

Shadow-camera based solar nowcasting system for shortest-term forecasts

Pascal Kuhn[1], Dominik Garsche[1], Stefan Wilbert[1*], Bijan Nouri[1], Natalie Hanrieder[1], Christoph Prahl[1], Luis Zarzarlejo[2], Jesús Fernández[3], Andreas Kazantzidis[4], Thomas Schmidt[5], Detlev Heinemann[5], Philippe Blanc[6] and Robert Pitz-Paal[7]

[1]German Aerospace Center (DLR), Institute of Solar Research, Institute of Solar Research, Tabernas, Spain
[2]CIEMAT, Energy Department – Renewable Energy Division, Madrid, Spain
[3]CIEMAT-Plataforma Solar de Almería, Tabernas, Almería, Spain
[4]Laboratory of Atmospheric Physics, Department of Physics, University of Patras, Patras, Greece
[5]German Aerospace Center (DLR), Institute of Networked Energy Systems, Oldenburg, Germany
[6]MINES ParisTech, PSL Research University, O.I.E. Centre Observation, Impacts, Energy, Sophia Antipolis CEDEX, France
[7]German Aerospace Center (DLR), Institute of Solar Research, Cologne, Germany.

Abstract

The rapid growth of solar power generation and the variable nature of the solar resource pose challenges for our electricity grids. Forecasting future changes in the irradiance might help to cost-efficiently manage this variability both for photovoltaic and concentration solar plants as well as grids with high solar penetrations. So far, for shortest-term forecasts with lead times of a few minutes, all-sky imager based nowcasting systems are used. However, due to the complexity of dynamically changing 3d cloud shapes as well as certain geometrical effects such as self-occlusion or near-horizon saturation, all-sky imager based nowcasting systems exhibit inherent weaknesses. Here, we present a novel system to generate shortest-term solar forecasts, which is located at Plataforma Solar de Almería in southern Spain. This approach is based on downward-facing cameras (shadow cameras), taking images of the ground. From these images, spatially resolved irradiance maps are derived. By tracking cloud shadows, future irradiances are predicted. A demonstration system is achieved, which provides shortest-term forecasts for the next 2 min. To the best of our knowledge, this is the first time such a system is developed. We benchmark several possible algorithmic approaches on 16 days and compare the deviations to a state-of-the-art all-sky imager based nowcasting system on 22 days. The root-mean-squared deviation (RMSD) of this shadow camera based nowcasting system for direct normal irradiance (DNI) and 1-min temporal averages is 15.6 % for lead times of 2 min (MAD, DNI: 9.6 %). In comparison to an all-sky imager system, this is an improvement as the all-sky imager system only reaches 22.0 % RMSD and 14.8 % MAD (both DNI). This demonstrates the feasibility and attractiveness in terms of accuracy of the proposed concept.

Keywords: Solar nowcasting, energy meteorology, meteorological cameras, forecasting

1 Introduction

The generation of solar power depends on the current solar irradiance. Transient clouds can cause rapid declines in solar irradiance, which relates to quick drops in power dispatched by photovoltaic (PV) plants and pose operational challenges for solar thermal plants. As solar penetrations in many countries rise, the variability of the solar resource threatens the stability of electricity grids. Therefore, countries and grid operators have started to define maximum ramp rates. For instance, Puerto Rico introduced a 10 % capacity per minute limit on PV ramp rates (Lave et al., 2013) and several grid operators in Australia established a 12 min ramp time, which means that a ramp down from the nominal rated output must be smoothened over 12 min (e.g., Rotstein et al., 2012). Shortest-term forecasts can cost-efficiently reduce the implementation costs of these regulations by allowing dynamic curtailment. There are numerous ways to forecast solar irradiances (e.g. Mellit, 2008; Inman, 2012; Inman et al., 2013; Antonanzas et al., 2016) and this section is confined to brief introductions with a focus on camera-based approaches.

Such shortest-term solar forecasts cannot be provided by numerical weather models (NWP, Mathiesen and Kleissl, 2011), having temporal resolutions of e.g. 3 h and spatial resolutions of several km^2 (e.g. Dragani et al., 2014). Furthermore, although the temporal and spatial resolutions of weather satellites are improving (e.g., Bley and Deneke, 2013; Bessho et al., 2016; Yoo et al., 2017), their resolutions are still too coarse for certain applications (Hammer et al., 1999; Cros et al., 2014).

*Corresponding author: Stefan Wilbert, German Aerospace Center (DLR), Institute of Solar Research, Tabernas, Spain

Additionally, solar irradiances can be predicted using other configurations. Various publications present forecasting methods based on radiometer measurements, often in combination with persistence forecasts (e.g., LARSON et al., 2016), statistical models (e.g., SHAKYA et al., 2017; MIAO et al., 2018), machine learning (e.g. PEDRO and COIMBRA, 2012; BENALI et al., 2018) or a combination thereof (PELLAND et al., 2011; ZAMO et al., 2014). Persistence forecasts extrapolate current measurements into the future while taking changes in irradiances caused by the future sun position into account (RAMIREZ et al., 2017). With the rising availability of measurements from large and distributed PV modules, much work is especially conducted in order to derive forecasts using such data (e.g., CHU et al., 2015; NUÑO et al., 2018; OGLIARI et al., 2018). For instance, CHEN et al. (2011) presents a 24 h PV power forecasting system based on measured meteorological parameters and the mean daily power output of the PV system using a neural network and a self-organized map to classify the weather forecasts provided by online meteorological services. Another approach is to utilize grids of irradiance sensors to derive short-term forecasts, e.g. as presented in SCHENK et al. (2015), YANG et al. (2015) and WANG et al. (2016). All of these statistical approaches cannot truely predict future shading events, which is possible with the novel methodology introduced in this paper.

Also, further methods based on publically available data are proposed, e.g. using weather forecasts from public websites (TAO et al., 2010) or meteorological data derived from public webcams (e.g. BRUNSKILL and JONES, 2011; KUHN et al., 2018d). Moreover, weather radars could be used to derive solar forecasts (e.g., PABLOS-VEGA et al., 2010; BIXEL, 2015). However, this instrumentation is relatively expensive and suffers from certain limitations regarding resolution and occlusion.

As of today, industrial camera-based nowcasting systems, providing shortest-term forecasts for the next minutes ahead with high spatial and temporal resolutions, are based on all-sky imagers (ASI). A large amount of all-sky imager based systems and approaches is presented in the literature (e.g. SHIELDS et al., 1998 (introduction of dedicated ASI hardware), SHAW et al., 2005 (demonstration of infra-red (IR) ASI), SMITH and TOUMI (2008) (demonstration of IR ASI), CHOW et al. (2011) (shadow nowcasting using a developed ASI), WOOD-BRADLEY et al. (2012) (cloud tracking approaches for ASI), URQUHART et al. (2012) (ASI derived nowcasts for PV), TOHSING et al. (2013) (ASI based sky luminance measurements), URQUHART et al. (2013) (overview of ASI applications and algorithms), HUANG et al. (2013) (ASI derived predictions of solar irradiance fluctuations), YANG et al. (2014) (development and validation of ASI derived global horizontal irradiance (GHI) nowcasts), ALONSO and BATLLES (2014) (comparison between weather satellite and ASI derived cloud coverages), CHU et al. (2014) (ASI based weather classifications for GHI forecasts), TOHSING et al. (2014) (ASI de-

rived spectral sky radiance measurements), BERTIN et al. (2015) (IR ASI for predicting optical satellite communication link availability), MASSIP et al. (2015) (presentation of nowcasting algorithms), PENG et al. (2015) (cloud detection and tracking using three ASIs), KILLIUS et al. (2015) (study on potential combination of ASI and NWP derived cloud heights), URQUHART et al. (2015) (introduction of high dynamic range (HDR) ASI for short-term solar power forecasting), NGUYEN et al. (2016) (using high resolution PV generation profiles from ASI for grid operators), WILBERT et al. (2016) (DNI nowcasts derived from four ASIs), SCHMIDT et al. (2016) (GHI nowcasts derived from one ASI and a ceilometer), SCHMIDT (2016) (ASI derived PV forecasts), ROY (2016) (design and installation of an ASI for PV nowcasts), KLEISSL et al. (2016) (field study using a developed ASI), WANG et al. (2016) (using one ASI and an additional sensor to measure cloud heights), KAZANTZIDIS et al. (2017) (overview of ASI hardware and algorithms), KURTZ et al. (2017) (study on origin of ASI deviations), LIANDRAT et al. (2017) (cloud coverage nowcasts based on an IR ASI), KUHN et al. (2017b) (validation of a nowcasting system consisting of four ASIs), NOURI et al. (2018) (voxel-carving approach using four ASIs), BLANC et al. (2017) (DNI nowcasts derived from two ASIs), SCHMIDT (2017) (overview of algorithmic approaches), SALEH et al. (2018) (using an ASI to avoid batteries in PV plants), CRISOSTO et al. (2018) (GHI one hour ahead predictions in one-minute resolution using Artificial Neural Networks)).

Here, we demonstrate the feasibility of a novel concept: Instead of using upward-facing all-sky imagers, taking images of the sky, downward-facing off-the-shelf surveillance cameras are used. From an elevated position, these so-called shadow cameras take images of the ground on a solar test site (Plataforma Solar de Almería) in southern Spain. From these images and additional sensors, spatially resolved irradiance maps are generated. Based on derived cloud shadow speeds, future shadow positions and irradiance maps are predicted. The focus in this paper is on DNI nowcasts with lead times up to 2 min. GHI forecasts would also be possible using the same approaches.

The shadow camera system without nowcasting capabilities is introduced in KUHN et al. (2017a). A case study for a hypothetical shadow camera based nowcasting system is presented in KUHN et al. (2018a). Novel differential shadow tracking methods for shadow cameras are developed in KUHN et al. (2018c) and applied in KUHN et al. (2018b). As far as we know, there is no previous work on such systems from other groups and this is the first time a shadow camera based nowcasting system is realized.

Given the availability of an elevated position, we see for example the following possible applications for shadow camera based systems: (1) In (small) diesel-PV-hybrid plants, such shortest-term forecasts could be applied to timely trigger back-up generators (PETERS et al., 2018) and could thus replace, to some extent, more ex-

Meteorol. Z. (Contrib. Atm. Sci.)
PrePub Article, 2019

P. Kuhn et al.: Shadow camera based nowcasting system

3

pensive batteries, which are otherwise needed (SALEH et al., 2018). (2) High-resolution irradiance forecasts on a valley-scale area (e.g. 314 km² as modelled in KUHN et al., 2018a) could be used to extract findings from a limited considered area and apply them to a wider region. This might potentially be feasible for derived cloud motion vectors and solar variability classes, which may be similar over larger distances. (3) Shadow camera based shortest-term forecasts could also improve operations in industrial concentration solar (NOURI et al., 2018) and PV power plants (WATSON et al., 2018). (4) Additionally, shadow cameras systems could provide reference measurements for e.g. NWP or satellite derived cloud (shadow) motion vectors, cloud sizes and cloud dynamics. Finally, such easy-to-operate systems could be used for solar site assessments.

This publication is structured as follows: In section 2, the shadow camera system is briefly introduced. Furthermore, improvements of the shadow camera system in comparison to the version presented in KUHN et al. (2017a) are explained. In section 3, the implementation of the nowcasting capabilities into the shadow camera system is shown. Several competing algorithmic approaches are considered. These approaches are benchmarked against each other in section 4. Moreover, the shadow camera based nowcasting system is benchmarked against a state-of-the-art all-sky imager based nowcasting system. The conclusion is given in section 5.

2 Summary and improvement of the existing shadow camera system

2.1 Summary of the previously existing shadow camera system

The hardware and configuration of the shadow camera system further developed here is originally presented and validated for current irradiance maps in KUHN et al. (2017a). The system consists of six downward-facing cameras, two of which are shown in Figure 1. These cameras are located at a height of 87 m on CIEMAT's CESA-I tower at the Plataforma Solar de Almería in southern Spain. From this elevated position, these six cameras take images of the ground with an image acquisition rate of 15 s (see example image in Figure 2). With the known exterior and internal orientation, a so-called orthoimage is generated from the six jpg images. This orthoimage covers an area of 2 km × 2 km with a spatial resolution of 5 m × 5 m (temporal resolution: 15 s).

Using two reference orthoimages, corresponding to similar solar positions but taken when (1) the whole imaged area was unshaded (*sunny reference orthoimage*) and (2) shaded (*shaded reference orthoimage*), cloud shadows are detected and spatially resolved irradiance maps are derived. For this, additional inputs of a meteorological station, namely DNI and diffuse horizontal irradiance (DHI) measurements corresponding to the

Figure 1: Two of the six shadow cameras on top of an 87 m high tower (CIEMAT's CESA-I) tower at the Plataforma Solar de Almería in southern Spain.

timestamps of the orthoimages, are used. In-depth explanations of this system, which previously could not provide forecasts, are given in KUHN et al. (2017a). Advantages and disadvantages of a hypothetical shadow camera based nowcasting system in comparison to all-sky imager based systems were discussed in KUHN et al. (2017a), section 5. These advantages are briefly summarized here:

1. Overexposed areas around the sun, which appear in all-sky images, are not a problem for downward-facing shadow cameras.

2. The derivation of cloud heights, needed for many all-sky imager systems (KUHN et al., 2018b), is not required for shadow camera based nowcasting systems. Thus, this origin of deviations is completely avoided.

3. As the sun light reaches the earth more or less in parallel, cloud shadows are 2d projections of the clouds on the ground. Therefore, shadow cameras, which directly image the shadows, do not suffer from self-occlusion effects of clouds. Due to self-occlusion, cloud coverages as perceived by all-sky imagers increase towards the horizon as gaps between clouds are occluded by neighboring clouds.

4. The 2d shadows are easier to track than 3d cloud objects, especially as in most situations ground-based all-sky imager cannot see the backside of the clouds and thus cloud shapes must be estimated.

5. Shadow cameras can directly measure the transmittance of a cloud by evaluating its shadow. Due to inter- and intra-cloud reflections, this is more challenging in all-sky images.

6. In comparison to all-sky imagers, maintenance and cleaning is much easier for downward-facing shadow cameras, especially regarding dust and bird droppings.

Figure 2: Photo from one shadow camera and the correction of the vignetting effect: jpg image (left), applied vignetting matrix (center) and corrected image (right).

7. One disadvantage of the used shadow camera configuration is its limited imaged area ($2\,\mathrm{km} \times 2\,\mathrm{km}$), which is far smaller than areas usually considered by all-sky imager based systems. This limitation can be overcome by using distributed shadow cameras, higher camera resolutions or camera positions with higher elevations.

Having summarized the advantages of shadow camera based nowcasting systems, we must mention that shadow cameras require (1) an elevated position and an area with (2) little non-cloud movements as well as (3) few shadows of elevated structures in which cloud shadows can be detected. Using the current configuration, shadows cannot be detected on highly reflective areas such as mirrors and difficulties in segmenting shadows directly on PV modules are expected. Although the focus here is on DNI, the shadow camera system can also derive GHI maps as e.g. validated in SCHENK et al. (2015).

2.2 Recent adaptions of the shadow camera system

2.2.1 Normalization and corrections of jpg images

Although off-the-shelf surveillance cameras (Mobotix M24 and M25) with overvoltage protection boxes (Ubiquiti) are used, lightning appears to be an issue and camera models had to be exchanged. Also, even same-model cameras have slightly different chips and exposure times, thus taking differently looking images. Therefore, we apply normalizations and corrections to the jpg images. This is done twofold: First of all, vignetting is determined and corrected (see Figure 2). Vignetting describes a darkening of the image towards the edges due to lens effects. In a second step, different cameras' brightness and contrasts are normalized among the shadow cameras to achieve a homogeneous orthoimage.

In literature, many approaches to correct vignetting are proposed (e.g. YU et al., 2004; KIM and POLLEFEYS, 2008; ZHENG et al., 2009; CHO et al., 2014). For our purposes, we found the approach suggested by ZHENG et al. (2008) to be feasible. In Figure 2, an example correction is shown. The vignetting matrix, once derived for every shadow camera following ZHENG et al. (2008), is applied to the jpg image, brightening the edges of the image. The normalization of the jpg images is conducted by generating look-up tables from pixels seen by two cameras and thus correcting offsets.
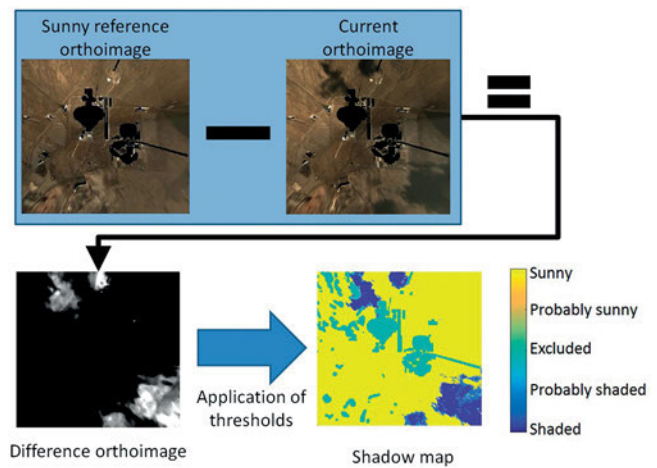

Figure 3: Flow chart of the previous shadow segmentation, described in KUHN et al. (2017a): A difference image is calculated from the current orthoimage and the corresponding sunny reference orthoimage. By applying thresholds, shadows are segmented. Certain pixels corresponding e.g. to buildings are excluded from further evaluation and later interpolated.

2.2.2 Adaptions of the optional segmentation into shaded and unshaded areas

We investigated three different methods to infer DNI maps from shadow maps. Two of these approaches are based on a prior segmentation of the imaged area into shaded and unshaded areas. The third method directly calculates DNI values from a set of images.

Figure 3 depicts the flow chart of the segmentation of the current orthoimage into shaded and unshaded areas as described in KUHN et al. (2017a): Based on the difference between the current orthoimage and the sunny reference orthoimage, a difference image is calculated. By applying a fixed threshold, this difference orthoimage is segmented into several classes, including *sunny* and *shaded* (the other classes are subsequently assigned to these two classes). For the areas classified as unshaded, the method from HANRIEDER et al. (2016) is used, which analyses the temporal variation of the Linke turbidity to derive a clear sky irradiance value. This clear sky model also takes the changes in the clear sky irradiance due to the sun's movements for lead times greater $0\,\mathrm{min}$ into account. The irradiance values for the shaded areas are derived from camera images as described in KUHN et al. (2017a). The approach used shaded and unshaded reference images as well as corresponding irradiance measurements to derive irradiance from the pixel values of current shadow cameras' images.

To improve the robustness of this segmentation, the approach is adapted. In this adapted approach, differences images to the current orthoimage are calculated from both the sunny and shaded reference orthoimage (Diff. image$_{\mathrm{Sunny2Current}}$ and Diff. image$_{\mathrm{Shaded2Current}}$). Also, the segmentation is reduced to the two relevant classes (*sunny* and *shaded*).

Figure 4: Flow chart of the shadow camera based nowcasting system. Based on camera images and meteorological data, the current irradiance map is derived. With additional tracking of cloud shadow motion vectors, future irradiance maps are predicted.
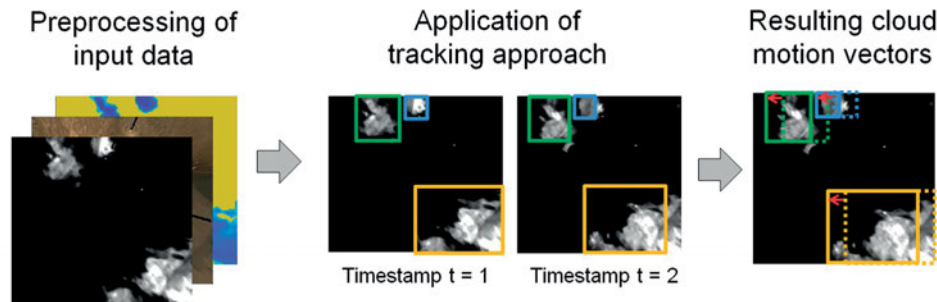

Figure 5: Flow chart of a tracking process: Firstly, input data must be preprocessed, e.g. by applying normalization and corrections to the jpg images or shadow segmentation. Afterwards, the tracker is applied, which derives cloud motion vectors.

The new segmentation algorithm segments a pixel in the current orthoimage to be unshaded if the difference between this pixel and the corresponding pixel in the sunny reference orthoimage is three times larger than the difference to the shaded orthoimage ($3 \times \text{Diff. image}_{\text{Sunny2Current}} < \text{Diff. image}_{\text{Shaded2Current}}$). This ratio was determined empirically. Otherwise, the pixel is classified as shaded. Unlike the previous algorithm, this approach does not depend on a fixed threshold but is relative to both reference orthoimages.

Besides this adapted approach, the calculation of irradiance maps without prior shadow segmentation based on eg. 16 in KUHN et al. (2017a) for all pixels is studied. This equation derives irradiances from current camera images by comparing them to reference images and corresponding DNI and DHI measurements.

3 Development of a shadow camera based nowcasting system

Using the initial shadow camera system and the adaptions described in section 2, a forecasting capability is implemented into the system. In Figure 4, the work flow of this shadow camera based nowcasting system is shown: Required inputs are the images taken by the shadow cameras and additional measurement data from a meteorological station. Corrections and normalizations might be applied on the jpg images (see section 2.2.1). Afterwards, shadows are segmented in the current orthoimage (see section 2.2.2). With methods described in KUHN et al. (2017a), irradiance maps are generated. In this publication, we will focus on DNI maps. The system can also produce GHI maps (shown in KUHN et al., 2017a).

In order to predict future irradiance maps, cloud shadows are tracked and the derived shadow motion vectors are used for extrapolating future shadow positions. This is explained in section 3.1. We will specifically look at global (section 3.1.1) and local tracking methods (section 3.1.2), using several trackers.

3.1 Considered tracking approaches

Figure 5 shows the general work flow for tracking: First of all, the input data must be preprocessed, e.g. by generating difference images. Then the tracking approach is applied, which finally leads cloud motion vectors.

Many tracking approaches are presented in the literature (YILMAZ et al., 2006; YANG et al., 2011; WU et al., 2015). Based on the results of the Visual Object Tracking Challenge (KRISTAN et al., 2017), we confine ourselves to the *Kernelized Correlation Filter-* (KCF, HENRIQUES et al., 2015), *Staple-* (BERTINETTO et al., 2015) and the *Discriminative Correlation Filter with Channel and Spatial Reliability* (CSR-DCF, LUKEZIC et al., 2017) tracker.

The KCF-tracker as developed by HENRIQUES et al. (2015) uses as inputs a bounding boxes around an object in the current frame. In the following frame, areas within the image are assigned a probability of containing this object using ridge regression and a circular matrix containing virtual images of the translated object. This circular matrix can be Fourier transformed, which significantly reduces computational costs.

The Staple-tracker (BERTINETTO et al., 2015) uses both circular matrices and histograms to detect objects and their corresponding bounding boxes. Both approaches individually derive probabilities, which are afterwards combined with a manually specified weighting
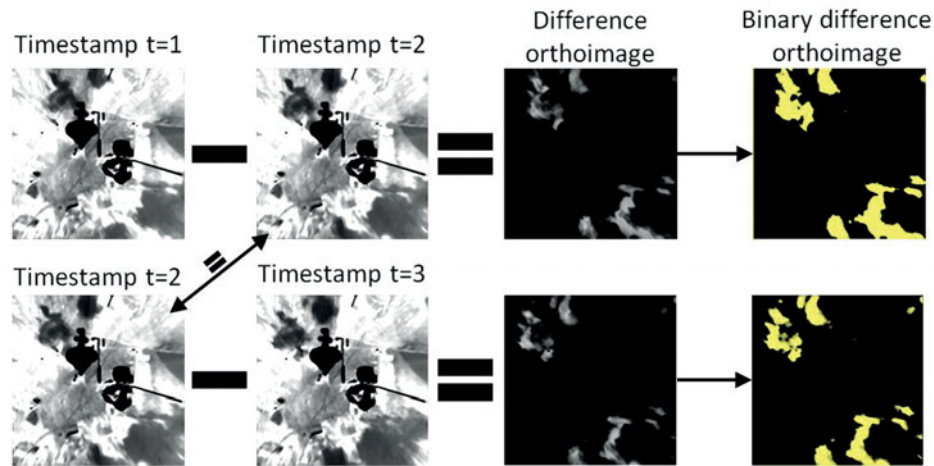
Figure 6: Working principle of the global tracking method: A series of three grayscale orthoimages, taken 15 s apart, is used to derive cloud motion vectors by subtracting concurrent orthoimages. The difference images are then segmented into binary difference images, which are used as inputs for the applied trackers to determine one global cloud motion vector. The same principle is used in the local tracking method to provide inputs for trackers deriving individual cloud shadow motion vectors.

factor α. As the histogram of an imaged object is less dependent on deformations, this additional input may outperform in certain situations approaches based on circular matrices. In the Visual Object Tracking challenges 2015–2017, the Staple-tracker yielded better results than the KCF-tracker at higher computational costs.

The CSR-DCF-tracker (Lukezic et al., 2017) complements the KCF-tracer by estimating the reliability both of individual pixels and of features. The this way weighed probabilities are combined to determine the position of the tracked object with the highest likeliness.

For all trackers, feasible configurations are derived by scrutinizing an example day (2015-09-19), specifically looking at *Histogram of Oriented Gradients*-features (HOG, Dalal and Triggs, 2005) and the grayscale orthoimage. For the KCF- and the Staple-tracker, the most promising results were obtained by HOG-features. For the CSR-DCF-tracker, both HOG-features and the grayscale orthoimage are used. The used settings are specified in the appendix. The implementations of the trackers can be found in Visual Object Tracking Challenge 2017 (2017).

The CSR-DCF- and the Staple-tracker are able to detect size variations in the tracked objects. However, due to the limited imaged area such scaling has negative impacts on the results and is deactivated in both trackers.

3.1.1 Global tracking method

For the global tracking method, one cloud shadow motion vector for all cloud shadows visible in the area imaged by the shadow camera system (2 km × 2 km) is derived. The working principle is shown in Figure 6. This differential approach uses three concurrent orthoimages, each taken 15 s apart. Subtractions lead to difference images, which serve as inputs for tracking algorithms.

Both the KCF- and the CSR-DCF-tracker are able to derive a cloud motion vector from these two grayscale differential input orthoimages. The Staple-tracker was found to struggle if the derived bounding boxes are partially outside the imaged area. Thus, for the global tracking method, only the KCF- and the CSR-DCF-tracker are used. A Kalman-filter considering data from previous timestamps is applied to the derived motion vectors to exclude outliers and to increase robustness.

3.1.2 Cloud shadow individual tracking method

In contrast to the global tracking method, which derives one general cloud motion vector for all cloud shadows visible in the imaged area, the cloud shadow individual (local) tracking method determines, if possible, individual shadow motion vectors.

For this tracking method, both inputs from the differential approach based on three concurrent orthoimages (similar to the approach used for the global tracking) and inputs based on the difference image between the current orthoimage and the sunny reference orthoimage are used. In Figure 7, the working principle of the local tracking method using the sunny reference orthoimage is shown. Within certain inputs (here: difference image of the current and the sunny reference orthoimage), noise is removed and shadows are detected. These detected objects serve as the base of the used tracker, with which objects are re-detected in the following input image. Based on the detected bounding boxes, cloud shadow motion vectors (indicated by white arrows) are estimate. These motion vectors are, if possible, individually Kalman-filtered with data from previous timestamps corresponding to the same cloud shadows, and finally used to generate nowcasts.

If shadows are visible in the imaged area for the first time, no individual motion vector can be determined and the global motion vector (see section 3.1.1) is assigned to such shadows.
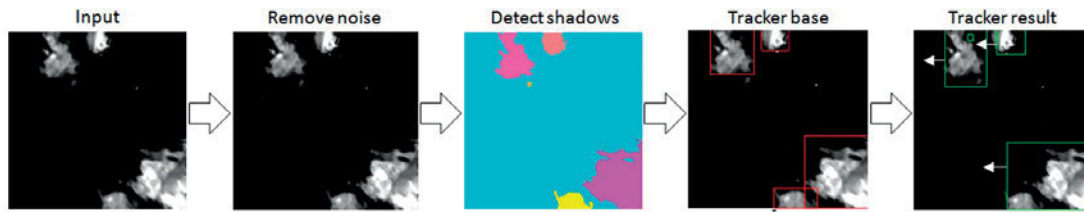
Meteorol. Z. (Contrib. Atm. Sci.)
PrePub Article, 2019

P. Kuhn et al.: Shadow camera based nowcasting system

7

Figure 7: Working principle of the shadow individual (local) tracking method using the sunny reference orthoimage: Individual shadow motion vectors are tracked based on shadows detected by subtracting the current (timestamp t_2) and previous orthoimage (timestamp t_1) with the corresponding sunny reference orthoimages. Differential images of three concurrent orthoimages can also be used as an input as shown for the global tracking method in Figure 6.
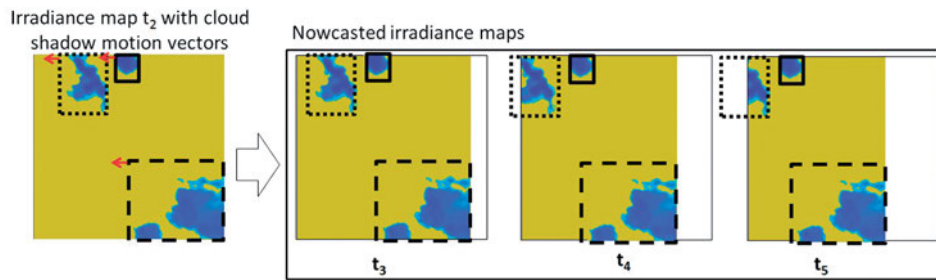
Figure 8: Working principle of the implemented nowcasting capability: From derived motion vectors and the current irradiance maps, future irradiance maps are forecasted. White areas in the nowcasted irradiance maps correspond to areas for which no forecast is possible.

3.2 Generation of nowcasted irradiance maps

Having determined the cloud shadow motion vectors, future irradiance maps are nowcasted by applying these motion vectors for the corresponding cloud shadow bounding boxes to the current irradiance map. Due to the limited imaged area, the area for which forecasts can be derived shrinks with higher lead times. The working principle is shown in Figure 8. If the current orthoimage is segmented into shaded and unshaded areas, the clear sky irradiance also used in KUHN et al. (2017b) is assigned to the unshaded areas. The irradiance values for the shaded areas are calculated from camera measurements as described in KUHN et al. (2017a) and translated based on cloud shadow motion vectors.

4 Evaluations and results

The evaluation of the shadow camera based nowcasting system is twofold: (1) In a first step, different configurations such as tracking and segmentation approaches of this system are compared to each other on 16 days. (2) In a second step, the thus determined optimal configuration is compared to an state-of-the-art all-sky imager based nowcasting system (WobaS-2cam) on 22 days. Visualizations of all days included in the benchmarks can be found in GARSCHE (2018). A qualitative assessment of all days is provided in Table 1. Timestamps with solar elevations below 15° are excluded due to the sun shining directly into the cameras' lenses for these situations (a mask was added later-on).

Table 1: Qualitative assessment of meteorological situation on days included in benchmarking periods of 16 and 22 days.

Day	Qualitative assessment
2015-09-19	scattered, thick clouds
2015-09-23	scattered, mainly thin clouds
2015-09-24	scattered to overcast, thick clouds
2015-09-26	scattered, thin clouds
2015-09-30	scattered to overcast, thick clouds
2015-10-03	overcast with breaks in the clouds
2015-10-04	scattered, thin and thick clouds
2015-10-05	scattered to overcast, thick clouds
2015-10-06	scattered, thin and thick clouds
2015-10-07	scattered, thin and thick clouds
2015-10-08	scattered, thick clouds
2015-10-27	scattered, thin and thick clouds
2015-10-28	scattered, thin clouds
2015-11-01	overcast with breaks in the clouds
2015-11-03	scattered, thin and thick clouds
2016-01-14	overcast with breaks in the clouds
	additional days for WobaS-2cam-comparison
2015-09-08	few thick clouds
2015-09-09	scattered, thin and thick clouds
2015-09-10	scattered, thin clouds
2015-09-11	scattered, thin and thick clouds
2015-09-15	few thin clouds
2015-09-18	few thick clouds

4.1   Evaluation approach and applied deviation metrics

Commonly, validations of solar nowcasting systems are conducted using conventional deviation metrics such as root-mean-square deviations (RMSD), mean-absolute deviations (MAD) and bias (eq. 4.1–4.3) compared to reference irradiance measurements from pyranometers or pyrheliometers, e.g. on 1-min temporal averages. Relative values are derived from absolute values and the average DNI as measured by the reference pyrheliometers.

$$\text{RMSD} = \sqrt{\frac{1}{N}\sum_{i=1}^{N}(\text{prediction}_i - \text{reference}_i)^2} \quad (4.1)$$

$$\text{MAD} = \frac{1}{N}\sum_{i=1}^{N}|\text{prediction}_i - \text{reference}_i| \quad (4.2)$$

$$\text{bias} = \frac{1}{N}\sum_{i=1}^{N}(\text{prediction}_i - \text{reference}_i) \quad (4.3)$$

However, as many authors have pointed out, conventional deviation metrics are not perfectly suited to validate forecasting systems (e.g. GILLELAND et al., 2009; SCHMIDT et al., 2016; VALLANCE et al., 2017; REMUND et al., 2017): A 1-min ramp, whose amplitude was correctly predicted, but two minutes too early, results in a so-called 'double-penalty' (GILLELAND et al., 2009) and the RMSD of this nowcasting system is far higher than the RMSD of a system which did not detect a ramp at all. However, for many industrial applications, a warning being too early might be better than no warning at all. This holds for instance in hybrid PV plants, in which the backup-generator needs time to ramp up.

Therefore, besides RMSD and MAD, we also consider the Temporal Distortion Index (TDI, FRÍAS-PAREDES et al., 2016) and the Ramp Tool and Metric, which is adapted from the wind energy sector for our solar purposes (BIANCO et al., 2016).

The TDI is calculated as follows: A cost matrix is determined by the absolute difference of all predictions and all reference irradiance measurements. The differences of the temporally matched predictions and measurements are on the diagonal of this $n \times n$ matrix with n being the number of predictions and measurements. The number of predictions and measurements does not have to be the same but is assumed to be this way to simplify discussions. All elements of this cost matrix outside the diagonal combine measurements with predictions made for another timestamp.

Through this cost matrix, the optimal path is found via dynamic programming. The optimal path is the path with the smallest sum of accumulated deviations. Boundary conditions apply (e.g. jumps are not allowed). The TDI is the area between the diagonal of the cost matrix and the optimal path. The greater the TDI, the bigger are the temporal offsets between the reference measure-
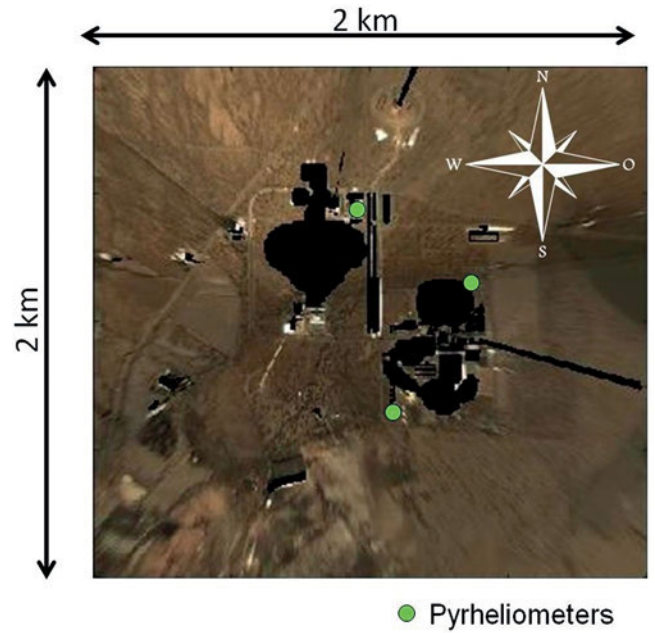

Figure 9: Positions of the pyrheliometers used in this evaluation inside the orthoimage.

ments and the predictions. The TDI is given as a percentage of the maximum possible temporal offset.

The comprehensive Ramp Tool and Metric (RT & M) is introduced in BIANCO et al. (2016) to validate wind forecasts. Here, it is adapted for solar forecasts and 1-min temporal averages. This tool is freely available on the internet (CIRES/NOAA, 2018) and uses three ramp definitions simultaneously to derive a ramp score: (1) The fixed-time interval method (Fixed Time), which determines ramps by the start and end values within a fix sliding time window, (2) the minimum-maximum method (Min-Max), which calculates ramps within a sliding time window between the local minimum and maximum and (3) the explicit derivative method (Derivative), which derives the ramps in a sliding time window based on the derivative form of the time series. A score is calculated based on the number of detected ramps as well as their temporal and irradiance alignment. The time window used here is 1 min.

4.2   Impact of the normalization of the jpg images on the nowcasts

Differences between the jpg images acquired by the shadow cameras are adapted by (1) applying a vignetting correction and (2) by normalization based on look-up tables (see section 2.2.1). In Figure 10, nowcasts using this normalization (*SC-normalization*) are compared to nowcasts without it, which is the so-called standard approach (*SC-standard*). For the nowcasts, the global tracking method with the CSR-DCF-tracker is used for both configurations.

For lead times of 0 min, only minor differences can be seen between the two implementations for the RMSD
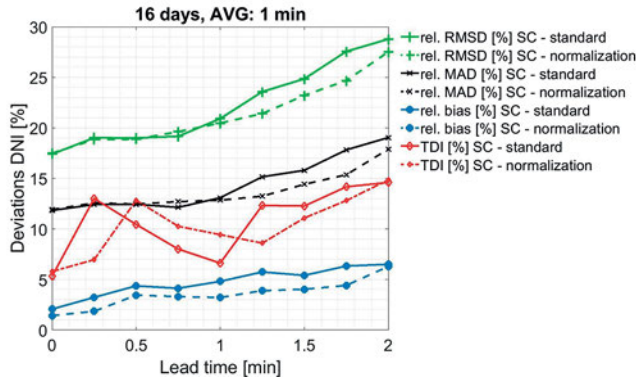
Meteorol. Z. (Contrib. Atm. Sci.)
PrePub Article, 2019

P. Kuhn et al.: Shadow camera based nowcasting system

9

Figure 10: Comparison of deviations of nowcasts with and without using jpg image adaptations. Adaptations are based on the correction of the vignetting effect and normalization between the cameras. Here, the previous segmentation approach and the global CSR-DCF-tracker are used. Other approaches lead to similar results.

Figure 11: Comparison of deviations of nowcasts using the previous segmentation approach and the differential segmentation explained in section 2.2.2 using the global CSR-DCF-tracker.

Figure 12: Comparison of deviations of nowcasted irradiance maps using the differential segmentation approach and without any shadow segmentation as well as a global CSR-DCF-tracker. In this approach, the irradiance of all pixels are derived from camera measurements. If shadow segmentation is applied, areas derived to be unshaded are assigned to have the clear sky irradiance value.

and the MAD in Figure 10. However, normalization reduces the RMSD and the MAD for higher lead times as well as the bias in general. The temporal distortion index (TDI) is similar for both approaches.

The reason for the reduced deviations for larger lead times originates from clouds being shifted into parts of the orthoimage imaged by other cameras. For the normalized images, the tracking of clouds becomes easier as the images, due to the normalization, are more alike. This effect is not visible for lead time 0 min as the corresponding irradiances are derived from images of the same camera and normalization between cameras is thus irrelevant.

In Figure 10, a moderate bias which rises with the lead times is present. This could indicate a bias in the cloud dynamics at PSA towards melting instead of forming clouds or a bias of the derived cloud shadow motion vectors towards lower speeds. Future work will study these hypotheses. With the found results, normalization is applied in the following.

4.3 Evaluation of nowcasts with different shadow segmentation approaches

In section 2.2.2, several approaches to use (or not use) shadow segmentation are explained. The nowcasts obtained with these approaches are compared to each other in Figure 11 and 12. In Figure 11, the previous segmentation (*SC-previous segmentation*) as used in KUHN et al. (2017a) is compared to a differential approach (*SC-differential approach*) described in section 2.2.2, yielding only minor differences.

In Figure 12, the differential segmentation is compared to an approach which does not apply shadow segmentation (*SC-no shadow segmentation*). If the imaged area in the current orthoimage is segmented into shaded and unshaded areas, a clear sky model is used for the unshaded areas. If no such segmentation is applied, the irradiance values for all pixels are derived from camera measurements as explained in section 2.2.2.
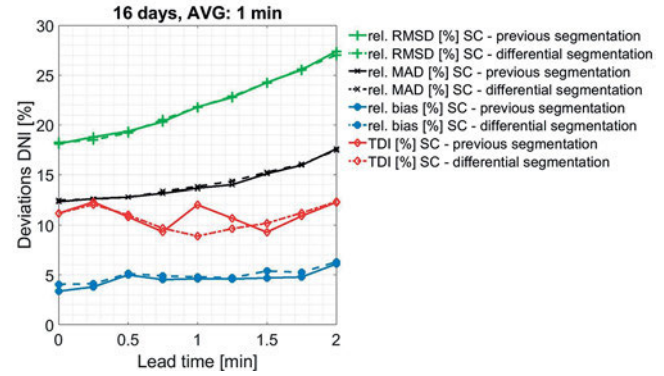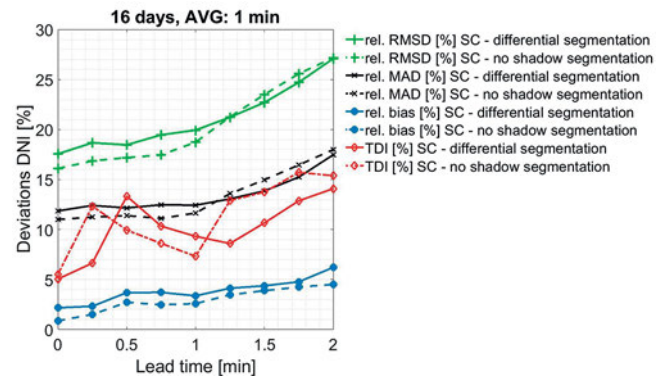
Figure 12 indicates that for lead times up to 75 s the approach without shadow segmentation is less prone to deviations in comparison to the differential or the previous segmentation approaches. Beyond lead times of 75 s, the segmentation approaches show marginally less deviations for MAD, TDI and RMSD. This can be explained by optically thin clouds, whose shadows are prone to be classified as unshaded areas, but can be determined to have irradiance values corresponding to bright shadows if no shadow segmentation is used. However, as optically thin clouds at high altitudes often have different motion vectors in comparison to lower clouds, forecasts tend to be less accurate once these optically thin clouds are detected. In addition to that, due to camera instabilities, not using shadow segmentation increases the noise levels in the irradiance maps. These effects might explain the behavior seen in Figure 12. In general, not using shadow segmentation is determined to be the better approach and is thus used in the following.

Table 2: Overview of the benchmarked tracking configurations.

tracking	inputs	tracker
global	3 concurrent orthoimages	CSR-DCF KCF
local	3 concurrent orthoimages	CSR-DCF KCF Staple
local	current, previous and corresponding sunny orthoimage	CSR-DCF KCF Staple

4.4   Evaluation of tracking algorithms

Here, we benchmark a total of eight tracking approaches on 16 days. These tracking approaches are (1) the CSR-DCF-tracker and (2) KCF-tracker, used to derive one global cloud shadow motion vector for the whole orthoimage (global tracking method). The (3) CSR-DCF-, (4) KCF- and (5) Staple-trackers are used to derive individual motion vectors for each shadow (local tracking method). All these approaches (1–5) are based on the differential approach, using difference images of three concurrent orthoimages. These difference orthoimages serve as inputs for the two global and three local trackers. For the local trackers, besides this differential approach, images calculated from subtractions of the current and previous orthoimages with their corresponding sunny reference orthoimages are additionally studied as inputs for the trackers (approaches 6–8). Table 2 provides an overview of the benchmarked tracking configurations.

Figure 13 depicts the deviations obtained with the CSR-DCF-tracker and the KCF-tracker for the global tracking method without shadow segmentation. Using the global approach, the irradiance map for lead time 0 min is taken as-is with minor deviations arising due to uncertainties in picking reference orthoimages, which are caused by minor server delays. For the local approach, clear sky irradiances are assumed for every pixel for which no cloud shadow was detected. Thus, the irradiance maps and deviations for lead time 0 min can be slightly different. These differences are considered to be irrelevant.

For lead times larger than 0 min, the KCF-tracker shows larger RMSD and MAD than the CSR-DCF-tracker. However, the bias found using the KCF-tracker is smaller. Similar comparisons find the CSR-DCF-tracker outperform the KCF-tracker for local tracking methods, considering individual cloud speeds (not shown). By a small margin, the CSR-DCF-tracker is outperformed by the Staple-tracker (not shown). If difference images calculated from the current and previous orthoimages and the corresponding sunny reference orthoimages are used as input data for the trackers, the KCF-tracker shows the smallest deviations of all shadow individual tracking methods.
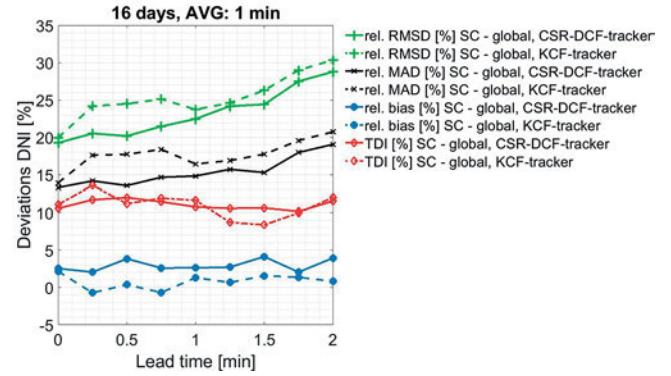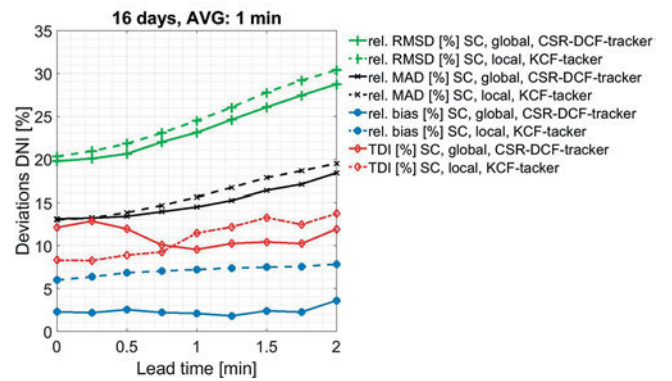

Figure 13: Comparison of deviations of nowcasts obtained with the CSR-DCF-tracker and the KCF-tracker for the global tracking method without shadow segmentation.

Figure 14: Comparison of deviations of nowcasts of the best global and best local tracking method.

Figure 14 compares the best global tracking method (differential approach combined with the CSR-DCF-tracker) with the best local tracking method (KCF-tracker applied on difference images to the sunny reference orthoimage). The global tracking method shows smaller deviations than the local tracking method but higher TDI for some lead times. This is caused by (1) the global tracking having more data for tracking, which makes deviations less likely. As the predictions are based on determined cloud shadow motion vectors, small deviations in the measured velocities and directions lead to deviations which increase with lead times. (2) Secondly, multi-layer cloud situations with overlapping shadows on the ground are found to be especially challenging for local tracking methods. Global tracking approaches, although only deriving one general motion vectors, yield less deviations in such complex situations. This is attributed to the larger database of global cloud shadow motion vectors in comparison to shadow individual motion vectors, which enables Kalman-filtering of outliers.

Similar challenges are present for all-sky imager based nowcasting systems. Hypothetically, shadow camera systems imaging larger areas might better cope with such multi-layer situations due the increased amount of available data for (individual) cloud tracking.
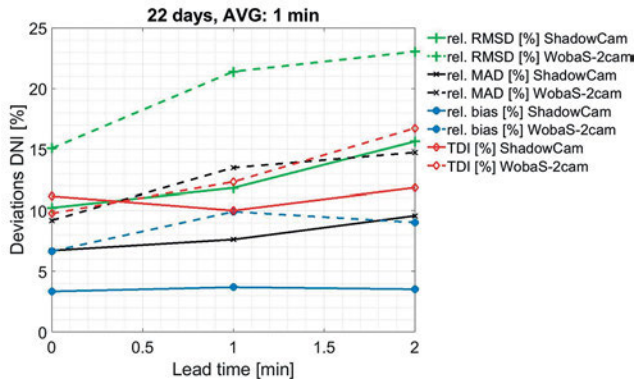
Meteorol. Z. (Contrib. Atm. Sci.)
PrePub Article, 2019

P. Kuhn et al.: Shadow camera based nowcasting system

11

Figure 15: Comparison of deviations of nowcasts of the all-sky imager based nowcasting system WobaS-2cam and the shadow camera based nowcasting system.

4.5 Benchmarking the shadow camera system against a state-of-the-art all-sky imager based nowcasting system

In Figure 15, the best configuration of the shadow camera based nowcasting system (global tracking method based on a differential approach from three concurrent orthoimages in combination with the CSR-DCF-tracker without additional shadow segmentation) is compared on 22 days to the state-of-the-art WobaS-2cam system, which is an all-sky imager based nowcasting system using two upward-facing cameras. WobaS-2cam provides a set of nowcasts with lead times of 0, 1, 2, . . . 15 min every 30 s. To compare the two systems, WobaS-2cam forecasts with lead times of 0 min, 1 min and 2 min are compared to shadow camera based forecasts of the same lead times and timestamps. Working principles of this system are explained in Nouri et al. (2019).

For lead times of 0 min, the deviations found for DNI and the shadow camera system (RMSD: 10.2 %, MAD: 6.7 %) are lower than the deviation of WobaS-2cam (RMSD: 15.1 %, MAD: 9.2 %), meaning that the base of the shadow camera nowcasts is more accurate. Notably, the bias found for the shadow camera system (3.3 %) is smaller than the bias of WobaS-2cam (6.7 %). Similar patterns are found for lead times of 2 min, with the shadow camera system yielding 15.6 % RMSD and 9.6 % MAD while WobaS-2cam results in 22.0 % RMSD and 14.8 % MAD.

The shadow camera based nowcasting system achieves a higher score using the Ramp Tool & Metric (Bianco et al., 2016): The higher score visible in Figure 16 indicates more accurate ramp predictions in comparison to the WobaS-2cam system for all considered lead times. Detailled studies revealed that the largest differences in deviations between the two systems occure for days with variable cloud transmittances, which are more accurately measured by the shadow camera system. Therefore, the advantages of a shadow camera based nowcasting system in comparison to all-sky imager based systems (discussed in section 2.1) seem to result in smaller deviations and improved forecasts.

5 Conclusion and outlook

We presented a novel approach to derive solar shortest-term forecasts using downward-facing cameras, taking images of the ground. From these images, irradiance maps are derived and future irradiances are predicted up to 2 min ahead by tracking cloud shadows. To the best of our knowledge, this is the first time such a system is achieved.

Several algorithmic approaches to implement this novel concept are benchmarked. A configuration using a global tracking method based on a differential approach from three concurrent orthoimages in combination with the CSR-DCF-tracker without additional shadow segmentation is found to yield the least deviations in comparison to pyrheliometer measurements. This setup is compared to a state-of-the-art all-sky imager based nowcasting systems and found to outperform it. Reasons for this achievement as well as limitations of shadow camera based systems are discussed.

Main limitation of the current system is its small imaged area of 2 km × 2 km. Frequently, cloud shadow sizes are larger than this area. Furthermore, due to the speed of clouds, tracking can often only be conducted on a few concurrent images and cloud dynamics are difficult to model. Therefore, we plan to install a new shadow camera system on a near-by mountain ridge. This planned shadow camera system could have an imaged area of about 100 km^2.

Shadow cameras might enable research in a multitude of fields, including (1) studies of cloud dynamics, (2) long-term measurements of cloud motion vectors, which might be relevant for the validation of NWP or satellite products, and (3) solar shadow camera based nowcasts for the next minutes. Furthermore, (4) statistical effects such as the aperture problem, relevant for many speed estimating systems, can be investigated (as demonstrated in Kuhn et al., 2018c). To sum it up, shadow cameras appear to have great potential for a number of fields both in research and industry.
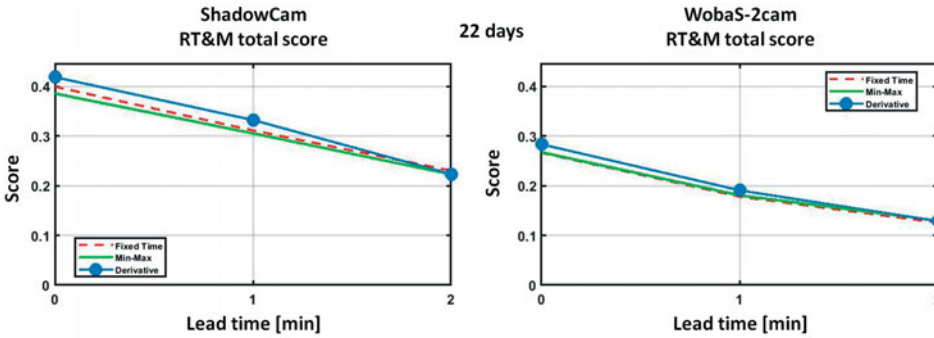
Acknowledgments

Figure 16: Comparison of deviations of nowcasts of the all-sky imager based nowcasting system WobaS-2cam and the shadow camera based nowcasting system using the Ramp Tool & Metric (Bianco et al., 2016).

Table A.1: Used parameters for the KCF-tracker.

Parameter	Value
Kernel type	Gaussian
Feature type	HOG
HOG Cell Size	4
Padding	1.5
Lambda	1e-4
Output Sigma Factor	0.01

Table A.2: Used parameters for the CSR-DCF-tracker.

Parameter	Value
Kernel type	Gaussian
Feature type	HOG und Gray
HOG Cell Size	4
Padding	1
Use scale	false
Output Sigma Factor	1

Table A.3: Used parameters for the Staple-tracker.

Parameter	Value
HOG Cell Size	4
Fixed Area	150^2
Number of bins	2^5
Feature type	NSAMF
Output Sigma Factor	0.5
Lambda	1e-3
Scale Adaptation	false
Merge factor	0.3
Merge Method	const. factor

Appendix

Parameters of the trackers   In Tables A.1–A.3, a list of the used tracker parameters is given. The implementations provided by the Visual Object Tracking Challenge 2017 (Kristan et al., 2017) are used. Parameters, which are not specified here, are not relevant for our application and do not have an impact on the tracking results. Specifically, parameters affecting scaling are not applied. Moreover, parameters which become relevant after more than two images are not used as the tracking conducted here is always based on two frames.

References

Alonso, J., F. Batlles, 2014: Short and medium-term cloudiness forecasting using remote sensing techniques and sky camera imagery. – Energy **73**, 890–897, DOI: 10.1016/j.energy.2014.06.101.

Antonanzas, J., N. Osorio, R. Escobar, R. Urraca, F.M. de Pison, F. Antonanzas-Torres, 2016: Review of photovoltaic power forecasting. – Solar Energy **136**, 78–111, DOI: 10.1016/j.solener.2016.06.069.

Benali, L., G. Notton, A. Fouilloy, C. Voyant, R. Dizene, 2018: Solar Radiation Forecasting using Artificial Neural Network and Random Forest Methods: Application to Normal Beam, Horizontal Diffuse and Global Components. – Renewable Energy **132**, 871–884, DOI: 10.1016/j.renene.2018.08.044.

Bertin, C., S. Cros, L. Saint-Antonin, N. Schmutz, 2015: Prediction of optical communication link availability: real-time observation of cloud patterns using a ground-based thermal infrared camera. – Proc. SPIE **9641**, 96410A–96410A–8, DOI: 10.1117/12.2194920.

Bertinetto, L., J. Valmadre, S. Golodetz, O. Miksik, P.H.S. Torr, 2015: Staple: Complementary Learners for Real-Time Tracking. – CoRR **abs/1512.01355**.

Bessho, K., K. Date, M. Hayashi, A. Ikeda, T. Imai, H. Inoue, Y. Kumagai, T. Miyakawa, H. Murata, T. Ohno, A. Okuyama, R. Oyama, Y. Sasaki, Y. Shimazu, K. Shimoji, Y. Sumida, M. Suzuki, H. Taniguchi, H. Tsuchiyama, D. Uesawa, H. Yokota, R. Yoshida, 2016: An Introduction to Himawari-8/9; Japan's New-Generation Geostationary Meteorological Satellites. – J. Meteor. Soc. Japan **94**, 151–183, DOI: 10.2151/jmsj.2016-009.

Bianco, L., I.V. Djalalova, J.M. Wilczak, J. Cline, S. Calvert, E. Konopleva-Akish, C. Finley, J. Freedman, 2016: A wind energy ramp tool and metric for measuring the skill of numerical weather prediction models. – Wea. Forecast. **31**, 1137–1156, DOI: 10.1175/WAF-D-15-0144.1.

Bixel, P.S., 2015: Method for predicting and mitigating power fluctuations at a photovoltaic power plant due to cloud cover. – US Patent App. 14/537,104.

Blanc, P., P. Massip, A. Kazantzidis, P. Tzoumanikas, P. Kuhn, S. Wilbert, D. Schüler, C. Prahl, 2017: Short-Term Forecasting of High Resolution Local DNI Maps with

Meteorol. Z. (Contrib. Atm. Sci.)
PrePub Article, 2019

P. Kuhn et al.: Shadow camera based nowcasting system

13

Multiple Fish-Eye Cameras in Stereoscopic Mode. – AIP Conference Proceedings **1850**, 140004, DOI: 10.1063/1.4984512.

BLEY, S., H. DENEKE, 2013: A threshold-based cloud mask for the high-resolution visible channel of Meteosat Second Generation SEVIRI. – Atmos. Measur. Techniques **6**, 2713–2723, DOI: 10.5194/amt-6-2713-2013.

BRUNSKILL, J., C. JONES, 2011: The bloomsburg weather viewer: A resource for integrating webcam and local weather station data into the introductory meteorology classroom. – Bull. Amer. Meteor. Soc. **92**, 956–963, DOI: 10.1175/2011BAMS3131.1.

CHEN, C., S. DUAN, T. CAI, B. LIU, 2011: Online 24-h solar power forecasting based on weather type classification using artificial neural network. – Solar Energy **85**, 2856 – 2870.

CHO, H., H. LEE, S. LEE, 2014: Radial Bright Channel Prior for Single Image Vignetting Correction. – In: D. FLEET, T. PAJDLA, B. SCHIELE, and T. TUYTELAARS (Eds.), Computer Vision – ECCV 2014, 189–202, Cham. Springer International Publishing.

CHOW, C.W., B. URQUHART, M. LAVE, A. DOMINGUEZ, J. KLEISSL, J. SHIELDS, B. WASHOM, 2011: Intra-hour forecasting with a total sky imager at the UC San Diego solar energy testbed. – Solar Energy **85**, 2881–2893, DOI: 10.1016/j.solener.2011.08.025.

CHU, Y., H.T. PEDRO, L. NONNENMACHER, R.H. INMAN, Z. LIAO, C.F. COIMBRA, 2014: A Smart Image-Based Cloud Detection System for Intrahour Solar Irradiance Forecasts. – J. Atmos. Ocean. Technol. **31**, 1995–2007, DOI: 10.1175/JTECH-D-13-00209.1.

CHU, Y., B. URQUHART, S.M. GOHARI, H.T. PEDRO, J. KLEISSL, C.F. COIMBRA, 2015: Short-term reforecasting of power output from a 48 MWe solar PV plant. – Solar Energy **112**, 68–77.

CIRES/NOAA, 2018: Download CIRES/NOAA Ramp Tool and Metric.

CRISOSTO, C., M. HOFMANN, R. MUBARAK, G. SECKMEYER, 2018: One-hour prediction of the global solar irradiance from all-sky images using artificial neural networks. – Energies **11**, 2906.

CROS, S., O. LIANDRAT, N. SÉBASTIEN, N. SCHMUTZ, 2014: Extracting cloud motion vectors from satellite images for solar power forecasting. – In: 2014 IEEE Geoscience and Remote Sensing Symposium, 4123–4126. DOI: 10.1109/IGARSS.2014.6947394.

DALAL, N., B. TRIGGS, 2005: Histograms of oriented gradients for human detection. – In: 2005 IEEE Computer Society Conference on Computer Vision and Pattern Recognition (CVPR'05), volume 1, 886–893 vol. 1. DOI: 10.1109/CVPR.2005.177.

DRAGANI, R., S. ABDALLA, R.J. ENGELEN, A. INNESS, J.N. THÉPAUT, 2014: Ten years of ENVISAT observations at ECMWF: A review of activities and lessons learnt. – Quart. J. Roy. Meteor. Soc. **141**, 598–610, DOI: 10.1002/qj.2380.

FRÍAS-PAREDES, L., F. MALLOR, T. LEÓN, M. GASTÓN-ROMEO, 2016: Introducing the temporal distortion index to perform a bidimensional analysis of renewable energy forecast. – Energy **94**, 180 – 194, DOI: 10.1016/j.energy.2015.10.093.

GARSCHE, D., 2018: Entwicklung eines Schattenkamera-basierten Nowcasting-Systems für die Solarindustrie. – Master thesis, DLR/Hochschule für angewandte Wissenschaften München.

GILLELAND, E., D. AHIJEVYCH, B.G. BROWN, B. CASATI, E.E. EBERT, 2009: Intercomparison of spatial forecast verification methods. – Wea. Forecast. **24**, 1416–1430, DOI: 10.1175/2009WAF2222269.1.

HAMMER, A., D. HEINEMANN, E. LORENZ, B. LÜCKEHE, 1999: Short-term forecasting of solar radiation: a statistical approach using satellite data. – Solar Energy **67**, 139–150, DOI: 10.1016/S0038-092X(00)00038-4.

HANRIEDER, N., M. SENGUPTA, Y. XIE, S. WILBERT, R. PITZ-PAAL, 2016: Modeling beam attenuation in solar tower plants using common DNI measurements. – Solar Energy **129**, 244–255.

HENRIQUES, J.F., R. CASEIRO, P. MARTINS, J. BATISTA, 2015: High-speed tracking with kernelized correlation filters. – IEEE Transactions on Pattern Analysis and Machine Intelligence **37**, 583–596, DOI: 10.1109/TPAMI.2014.2345390.

HUANG, H., J. XU, Z. PENG, S. YOO, D. YU, D. HUANG, H. QIN, 2013: Cloud Motion Estimation for Short Term Solar Irradiation Prediction. – In: Smart Grid Communications (SmartGridComm), 2013 IEEE International Conference on, 696–701. IEEE, DOI: 10.1109/SmartGridComm.2013.6688040.

INMAN, R.H., 2012: Solar forecasting review. – Ph.D. thesis, UC San Diego.

INMAN, R.H., H.T. PEDRO, C.F. COIMBRA, 2013: Solar forecasting methods for renewable energy integration. – Progress in Energy and Combustion Science **39**, 535–576, DOI: 10.1016/j.pecs.2013.06.002.

ISO 9060, 1990: ISO 9060:1990, Solar energy – Specification and classification of instruments for measuring hemispherical solar and direct solar radiation. https://www.iso.org/standard/16629.html Accessed: 2018-09-25.

KAZANTZIDIS, A., P. TZOUMANIKAS, P. BLANC, P. MASSIP, S. WILBERT, L. RAMIREZ-SANTIGOSA, 2017: 5 – short-term forecasting based on all-sky cameras. – In: G. KARINIOTAKIS (Ed.), Renewable Energy Forecasting, Woodhead Publishing Series in Energy, Woodhead Publishing, 153–178, DOI: 10.1016/B978-0-08-100504-0.00005-6.

KILLIUS, N., C. PRAHL, N. HANRIEDER, S. WILBERT, M. SCHROEDTER-HOMSCHEIDT, 2015: On the use of NWP for Cloud Base Height Estimation in Cloud Camera-Based Solar Irradiance Nowcasting. – Oral presenation on EUPVSEC.

KIM, S.J., M. POLLEFEYS, 2008: Robust Radiometric Calibration and Vignetting Correction. – IEEE Transactions on Pattern Analysis and Machine Intelligence **30**, 562–576, DOI: 10.1109/TPAMI.2007.70732.

KLEISSL, J., B. URQUHART, M. GHONIMA, E. DAHLIN, A. NGUYEN, B. KURTZ, C. CHOW, F. MEJIA, 2016: University of California, San Diego (UCSD) Sky Imager Cloud Position Study Field Campaign Report. – Technical report, DOE ARM Climate Research Facility, Pacific Northwest National Laboratory; Richland, Washington.

KRISTAN, M., A. LEONARDIS, J. MATAS, M. FELSBERG, R. PFLUGFELDER, L.C. ZAJC, T. VOJÍR, G. HÄGER, A. LUKEŽIC, A. ELDESOKEY, G. FERNÁNDEZ, C. GARCÍA-MARTÍN, A. MUHIC, A. PETROSINO, A. MEMARMOGHADAM, A. VEDALDI, A. MANZANERA, A. TRAN, A. ALATAN, B. MOCANU, B. CHEN, C. HUANG, C. XU, C. SUN, D. DU, D. ZHANG, D. DU, D. MISHRA, E. GUNDOGDU, E. VELASCO-SALIDO, F.S. KHAN, F. BATTISTONE, G.R.K.S. SUBRAHMANYAM, G. BHAT, G. HUANG, G. BASTOS, G. SEETHARAMAN, H. ZHANG, H. LI, H. LU, I. DRUMMOND, J. VALMADRE, C.J. JEONG, I.J. CHO, J.Y. LEE, J. NOSKOVA, J. ZHU, J. GAO, J. LIU, J.W. KIM, J.F. HENRIQUES, J.M. MARTÍNEZ, J. ZHUANG, J. XING, J. GAO, K. CHEN, K. PALANIAPPAN, K. LEBEDA, K. GAO, K.M. KITANI, L. ZHANG, L. WANG, L. YANG, L. WEN, L. BERTINETTO, M. POOSTCHI, M. DANELLJAN, M. MUELLER, M. ZHANG, M.H. YANG, N. XIE, N. WANG, O. MIKSIK, P. MOALLEM, P.V. M, P. SENNA, P.H.S. TORR, Q. WANG, Q. YU, Q. HUANG, R. MARTÍN-NIETO, R. BOWDEN, R. LIU, R. TAPU, S. HADFIELD, S. LYU, S. GOLODETZ, S. CHOI, T. ZHANG, T. ZAHARIA, V. SANTOPIETRO, W. ZOU, W. HU, W. TAO, W. LI, W. ZHOU, X. YU, X. BIAN, Y. LI,

Y. Xing, Y. Fan, Z. Zhu, Z. Zhang, Z. He, 2017: The Visual Object Tracking VOT2017 Challenge Results. – In: 2017 IEEE International Conference on Computer Vision Workshops (ICCVW), 1949–1972. DOI: 10.1109/ICCVW.2017.230.

Kuhn, P., S. Wilbert, C. Prahl, D. Schüler, T. Haase, T. Hirsch, M. Wittmann, L. Ramirez, L. Zerzalejo, A. Meyer, L. Vuilleumier, P. Blanc, R. Pitz-Paal, 2017a: Shadow camera system for the generation of solar irradiance maps. – Solar Energy **157**, 157–170, DOI: 10.1016/j.solener.2017.05.074.

Kuhn, P., B. Nouri, S. Wilbert, C. Prahl, N. Kozonek, T. Schmidt, Z. Yasser, L. Ramirez, L. Zarzalejo, A. Meyer, L. Vuilleumier, D. Heinemann, P. Blanc, R. Pitz-Paal, 2017b: Validation of an all-sky imager-based nowcasting system for industrial PV plants. – Progress in Photovoltaics: Research and Applications **26**, 608–621, DOI: 10.1002/pip.2968 PIP-17-122.R1, cover article: 10.1002/pip.3065.

Kuhn, P., S. Wilbert, C. Prahl, D. Garsche, D. Schüler, T. Haase, L. Ramirez, L. Zarzalejo, A. Meyer, P. Blanc, R. Pitz-Paal, 2018a: Applications of a shadow camera system for energy meteorology. – Adv. Sci. Res. **15**, 11–14, DOI: 10.5194/asr-15-11-2018.

Kuhn, P., M. Wirtz, N. Killius, S. Wilbert, J. Bosch, N. Hanrieder, B. Nouri, J. Kleissl, L. Ramirez, M. Schroedter-Homscheidt, D. Heinemann, A. Kazantzidis, P. Blanc, R. Pitz-Paal, 2018b: Benchmarking three low-cost, low-maintenance cloud height measurement systems and ECMWF cloud heights against a ceilometer. – Solar Energy **168**, 140–152, DOI: 10.1016/j.solener.2018.02.050 Advances in Solar Resource Assessment and Forecasting.

Kuhn, P., M. Wirtz, S. Wilbert, J. Bosch, G. Wang, L. Ramirez, D. Heinemann, R. Pitz-Paal, 2018c: Field validation and benchmarking of a cloud shadow speed sensor. – Solar Energy **173**, 229–245, DOI: 10.1016/j.solener.2018.07.053.

Kuhn, P., F. Kammermeier, D. Bürkle, 2018d: Mit öffentlich zugänglichen Kameras wollen DLR-Forscher Stromnetze stabilisieren. https://www.dlr.de/dlr/desktopdefault.aspx/tabid-10081/151_read-29225/#/gallery/31599 Accessed: 2018-08-03.

Kurtz, B., F. Mejia, J. Kleissl, 2017: A virtual sky imager testbed for solar energy forecasting. – Solar Energy **158**, 753–759, DOI: 10.1016/j.solener.2017.10.036.

Larson, D.P., L. Nonnenmacher, C.F. Coimbra, 2016: Day-ahead forecasting of solar power output from photovoltaic plants in the American Southwest. – Renewable Energy **91**, 11–20.

Lave, M., J. Kleissl, A. Ellis, F. Mejia, 2013: Simulated PV power plant variability: Impact of utility-imposed ramp limitations in Puerto Rico. – In: 2013 IEEE 39th Photovoltaic Specialists Conference (PVSC), 1817–1821. DOI: 10.1109/PVSC.2013.6744495.

Liandrat, O., S. Cros, A. Braun, L. Saint-Antonin, J. Decroix, N. Schmutz, 2017: Cloud cover forecast from a ground-based all sky infrared thermal camera. – Proc.SPIE **10424**, 10424–10424–13, DOI: 10.1117/12.2278636.

Lukezic, A., T. Vojir, L.C. Zajc, J. Matas, M. Kristan, 2017: Discriminative Correlation Filter with Channel and Spatial Reliability. – In: Proceedings of the IEEE Conference on Computer Vision and Pattern Recognition, volume 2.

Massip, P., P. Blanc, A. Kazantzidis, P. Tzoumanikas, 2015: Report on algorithms for nowcasting methods based on sky imagers. – DNICast deliverable 3.1.

Mathiesen, P., J. Kleissl, 2011: Evaluation of numerical weather prediction for intra-day solar forecasting in the con-

tinental United States. – Solar Energy **85**, 967–977, DOI: 10.1016/j.solener.2011.02.013.

Mellit, A., 2008: Artificial Intelligence Technique for Modelling and Forecasting of Solar Radiation Data: a Review. – Int. J. Artif. Intell. Soft Comput. **1**, 52–76.

Miao, S., G. Ning, Y. Gu, J. Yan, B. Ma, 2018: Markov Chain model for solar farm generation and its application to generation performance evaluation. – J. Cleaner Production **186**, 905–917.

Nguyen, A., M. Velay, J. Schoene, V. Zheglov, B. Kurtz, K. Murray, B. Torre, J. Kleissl, 2016: High PV penetration impacts on five local distribution networks using high resolution solar resource assessment with sky imager and quasi-steady state distribution system simulations. – Solar Energy **132**, 221–235, DOI: 10.1016/j.solener.2016.03.019.

Nouri, B., P. Kuhn, S. Wilbert, C. Prahl, R. Pitz-Paal, P. Blanc, T. Schmidt, Z. Yasser, L.R. Santigosa, D. Heinemann, 2018: Nowcasting of DNI maps for the solar field based on voxel carving and individual 3D cloud objects from all sky images. – AIP Conference Proceedings **2033**, 190011, DOI: 10.1063/1.5067196.

Nouri, B., P. Kuhn, S. Wilbert, N. Hanrieder, C. Prahl, L. Zarzalejo, A. Kazantzidis, P. Blanc, R. Pitz-Paal, 2019: Cloud height and tracking accuracy of three all sky imager systems for individual clouds. – Solar Energy **177**, 213–228, DOI: 10.1016/j.solener.2018.10.079.

Nuño, E., M. Koivisto, N.A. Cutululis, P. Sorensen, 2018: On the Simulation of Aggregated Solar PV Forecast Errors. – IEEE Transactions on Sustainable Energy **9**, 1889–1898, DOI: 10.1109/TSTE.2018.2818727.

Ogliari, E., A. Niccolai, S. Leva, R.E. Zich, 2018: Computational Intelligence Techniques Applied to the Day Ahead PV Output Power Forecast: PHANN, SNO and Mixed. – Energies **11**, DOI: 10.3390/en11061487.

Pablos-Vega, G.A., J.G. Colom-Ustáriz, S. Cruz-Pol, J.M. Trabal, V. Chandrasekar, J. George, F. Junyent, 2010: Development of an Off-The-Grid X-band radar for weather applications. – 2010 IEEE International Geoscience and Remote Sensing Symposium 1077–1080.

Pedro, H.T., C.F. Coimbra, 2012: Assessment of forecasting techniques for solar power production with no exogenous inputs. – Solar Energy **86**, 2017–2028, DOI: 10.1016/j.solener.2012.04.004.

Pelland, S., G. Galanis, G. Kallos, 2011: Solar and photovoltaic forecasting through post-processing of the Global Environmental Multiscale numerical weather prediction model. – Progress in Photovoltaics: Research and Applications **21**, 284–296.

Peng, Z., D. Yu, D. Huang, J. Heiser, S. Yoo, P. Kalb, 2015: 3d cloud detection and tracking system for solar forecast using multiple sky imagers. – Solar Energy **118**, 496–519, DOI: 10.1145/2554850.2554913.

Peters, D., T. Kilper, M. Calais, T. Jamal, K. von Maydell, 2018: Solar Short-Term Forecasts for Predictive Control of Battery Storage Capacities in Remote PV Diesel Networks. – Springer International Publishing, Cham, 325–333, DOI: 10.1007/978-3-319-69844-1_29.

Ramirez, L., N. Hanrieder, S. Wilbert, L. Zarzalejo, J.M. Vindel, R.X. Valenzuela, M. Gastón, 2017: Report on Combination of nowcasted DNI. – DNICast deliverable 3.14.

Remund, J., L. Ramirez, S. Wilbert, P. Blanc, E. Lorenz, D. Renne, 2017: Solar resource for high penetration and large scale applications–a new joint Task of IEA PVPS and IEA SolarPACES. – Proceedings of the EU PVSEC 2017.

Rotstein, J., D. Edwards, A. Manjire, 2012: Technical Requirements for Renewable Energy Systems Connected to

Meteorol. Z. (Contrib. Atm. Sci.)
PrePub Article, 2019

P. Kuhn et al.: Shadow camera based nowcasting system

15

the Low Voltage (LV) Grid via Inverters. – Technical report, Horizon Power, available online at https://horizonpower.com.au/media/1281/hpc-9fj-12-0001-2012_-_std_-_technical_requirements_for_renewable_energy_systems_connected_to_the_lv_network_via_inverters-070217.pdf.

Roy, J.C.E., 2016: Design and installation of a Sky-camera network and data acquisition system for intra-hour solar irradiance and photovoltaic system output forecasting. – Ph.D. thesis, Murdoch University, available online at http://researchrepository.murdoch.edu.au/id/eprint/36738/.

Saleh, M., L. Meek, M.A.S. Masoum, M. Abshar, 2018: Battery-less short-term smoothing of photovoltaic generation using sky camera. – IEEE Transactions on Industrial Informatics 14, 403–414, DOI: 10.1109/TII.2017.2767038.

Schenk, H., T. Hirsch, M. Wittmann, S. Wilbert, L. Keller, C. Prahl, 2015: Design and Operation of an Irradiance Measurement Network. – Energy Procedia 69, 2019–2030, DOI: 10.1016/j.egypro.2015.03.212.

Schmidt, T., 2016: Abschlussbericht zur Machbarkeitsstudie von Kurzfristprognosen der solaren Einstrahlung am Beispiel der 1 MW PV-Anlage Solardach München-Riem. – SEV Bayern, available online at https://www.sev-bayern.de/content/downloads/Abschlussbericht_WolkenkameraRiem.pdf.

Schmidt, T., 2017: High resolution solar irradiance forecasts based on sky images. – Ph.D. thesis, Oldenburg University, available online at http://oops.uni-oldenburg.de/3232/1/schhig17.pdf.

Schmidt, T., J. Kalisch, E. Lorenz, D. Heinemann, 2016: Evaluating the spatio-temporal performance of sky-imager-based solar irradiance analysis and forecasts. – Atmos. Chem. Phys. 16, 3399–3412, DOI: 10.5194/acp-16-3399-2016.

Shakya, A., S. Michael, C. Saunders, D. Armstrong, P. Pandey, S. Chalise, R. Tonkoski, 2017: Solar Irradiance Forecasting in Remote Microgrids Using Markov Switching Model. – IEEE Transactions on Sustainable Energy 8, 895–905.

Shaw, J.A., P.W. Nugent, N.J. Pust, B. Thurairajah, K. Mizutani, 2005: Radiometric cloud imaging with an uncooled microbolometer thermal infrared camera. – Opt. Express 13, 5807–5817, DOI: 10.1364/OPEX.13.005807.

Shields, J., M. Karr, T. Tooman, D. Sowle, S. Moore, 1998: The Whole Sky Imager – A Year of Progress. – In: Eighth Atmospheric Radiation Measurement (ARM) Science Team Meeting, Tucson, Arizona, 23–27.

Smith, S., R. Toumi, 2008: Measuring Cloud Cover and Brightness Temperature with a Ground-Based Thermal Infrared Camera. – J. Appl. Meteor. Climatol. 47, 683–693, DOI: 10.1175/2007JAMC1615.1.

Tao, C., D. Shanxu, C. Changsong, 2010: Forecasting power output for grid-connected photovoltaic power system without using solar radiation measurement. – In: The 2nd International Symposium on Power Electronics for Distributed Generation Systems, 773–777. DOI: 10.1109/PEDG.2010.5545754.

Tohsing, K., M. Schrempf, S. Riechelmann, H. Schilke, G. Seckmeyer, 2013: Measuring high-resolution sky luminance distributions with a CCD camera. – Appl. Opt. 52, 1564–1573, DOI: 10.1364/AO.52.001564.

Tohsing, K., M. Schrempf, S. Riechelmann, G. Seckmeyer, 2014: Validation of spectral sky radiance derived from all-sky camera images – a case study. – Atmos. Measur. Techniques 7, 2137–2146, DOI: 10.5194/amt-7-2137-2014.

Urquhart, B., C.W. Chow, D. Nguyen, J. Kleissl, M. Sengupta, J. Blatchford, D. Jeon, 2012: Towards intra-hour solar forecasting using two sky imagers at a large solar power plant. – Proceedings of the American Solar Energy Society, Denver, CO, USA.

Urquhart, B., M. Ghonima, D.A. Nguyen, B. Kurtz, C.W. Chow, J. Kleissl, 2013: Chapter 9 – Sky-Imaging Systems for Short-Term Forecasting. – In: J. Kleissl (Ed.): Solar Energy Forecasting and Resource Assessment. – Academic Press, Boston, 195–232, DOI: 10.1016/B978-0-12-397177-7.00009-7.

Urquhart, B., B. Kurtz, E. Dahlin, M. Ghonima, J. Shields, J. Kleissl, 2015: Development of a sky imaging system for short-term solar power forecasting. – Atmos. Measur. Techniques 8, 875–890, DOI: 10.5194/amt-8-875-2015.

Vallance, L., B. Charbonnier, N. Paul, S. Dubost, P. Blanc, 2017: Towards a standardized procedure to assess solar forecast accuracy: A new ramp and time alignment metric. – Solar Energy 150, 408–422, DOI: 10.1016/j.solener.2017.04.064.

Visual Object Tracking Challenge 2017, 2017: VOT2017 Trackers repository. – http://votchallenge.net/vot2017/trackers.html Accessed: 2018-08-01.

Wang, G., B. Kurtz, J. Kleissl, 2016: Cloud base height from sky imager and cloud speed sensor. – Solar Energy 131, 208–221, DOI: 10.1016/j.solener.2016.02.027.

Watson, S., D. Bian, N. Sahraei, A.G.W. V, T. Buonassisi, I.M. Peters, 2018: Advantages of operation flexibility and load sizing for PV-powered system design. – Solar Energy 162, 132–139, DOI: 10.1016/j.solener.2018.01.022.

Wilbert, S., B. Nouri, P. Kuhn, D. Schüler, C. Prahl, N. Kozonek, R. Pitz-Paal, T. Schmidt, N. Killius, M. Schroedter-Homscheidt, Z. Yasser, 2016: Wolkenkamera-basierte Kürzestfristvorhersage der Direktstrahlung. – 19. Kölner Sonnenkolloquium, 6.7.2016, Cologne, Germany.

Wood-Bradley, P., J. Zapata, J. Pye, others, 2012: Cloud tracking with optical flow for short-term solar forecasting. – Solar Thermal Group, Australian National University, Canberra, Australia.

Wu, Y., J. Lim, M.H. Yang, 2015: Object Tracking Benchmark. – IEEE Transactions on Pattern Analysis and Machine Intelligence 37, 1834–1848, DOI: 10.1109/TPAMI.2014.2388226.

Yang, D., Z. Ye, L.H.I. Lim, Z. Dong, 2015: Very short term irradiance forecasting using the lasso. – Solar Energy 114, 314–326.

Yang, H., L. Shao, F. Zheng, L. Wang, Z. Song, 2011: Recent advances and trends in visual tracking: A review. – Neurocomputing 74, 3823–3831, DOI: 10.1016/j.neucom.2011.07.024.

Yang, H., B. Kurtz, D. Nguyen, B. Urquhart, C. Chow, M. Ghonima, J. Kleissl, 2014: Solar irradiance forecasting using a ground-based sky imager developed at UC San Diego. – Solar Energy 103, 502–524, DOI: 10.1016/j.solener.2014.02.044.

Yilmaz, A., O. Javed, M. Shah, 2006: Object Tracking: A Survey. – ACM Comput. Surv. 38, DOI: 10.1145/1177352.1177355.

Yoo, H., F. Yu, X. Wu, H. Qian, R. Iacovazzi, 2017: Assessing the GOES-16 ABI solar channels calibration using deep convective clouds. – Proc.SPIE 10403, 10403–10403–7, DOI: 10.1117/12.2275384.

Yu, W., Y. Chung, J. Soh, 2004: Vignetting distortion correction method for high quality digital imaging. – In: Proceedings of the 17th International Conference on Pattern Recognition, 2004. – ICPR 2004, volume 3, 666–669, DOI: 10.1109/ICPR.2004.1334617.

Zamo, M., O. Mestre, P. Arbogast, O. Pannekoucke, 2014: A benchmark of statistical regression methods for short-term forecasting of photovoltaic electricity production, part I: Deterministic forecast of hourly production. – Solar Energy 105, 792–803.

ZHENG, Y., J. YU, S.B. KANG, S. LIN, C. KAMBHAMETTU, 2008: Single-image vignetting correction using radial gradient symmetry. – In: 2008 IEEE Conference on Computer Vision and Pattern Recognition, 1–8, DOI: 10.1109/CVPR.2008.4587413.

ZHENG, Y., S. LIN, C. KAMBHAMETTU, J. YU, S.B. KANG, 2009: Single-Image Vignetting Correction. – IEEE Transactions on Pattern Analysis and Machine Intelligence **31**, 2243–2256, DOI: 10.1109/TPAMI.2008.263.